




Pulsed rise and growth of the Tibetan Plateau to its northern margin since ca. 30 Ma

Weitao Wang^{a,b,1}, Peizhen Zhang^{a,b}, Carmala N. Garzione^{c,d}, Caicai Liu^e, Zhuqi Zhang^e, Jianzhang Pang^e, Yizhou Wang^e, Dewen Zheng^f, Wenjun Zheng^{a,b}, and Huiping Zhang^e 

^aSchool of Earth Science and Geological Engineering, Sun Yat-Sen University, 510275 Guangzhou, China; ^bSouthern Marine Science and Engineering Guangdong Laboratory (Zhuhai), 519080 Zhuhai, China; ^cCollege of Science, University of Arizona, Tucson, AZ 85721; ^dDepartment of the Earth and Environment Sciences, University of Rochester, Rochester, NY 14627; ^eState Key Laboratory of Earthquake Dynamics, Institute of Geology, China Earthquake Administration, 100029 Beijing, China; and ^fState Key Laboratory of Isotope Geochemistry, Guangzhou Institute of Geochemistry, Chinese Academy of Sciences, 510640 Guangzhou, China

Edited by Lisa Tauxe, Scripps Institution of Oceanography, University of California San Diego, La Jolla, CA; received November 8, 2021; accepted January 11, 2022

The onset of mountain building along margins of the Tibetan Plateau provides a key constraint on the processes by which the high topography in Eurasia formed. Although progressive expansion of thickened crust underpins most models, several studies suggest that the northern extent of the plateau was established early, soon after the collision between India and Eurasia at ca. 50 Ma. This inference relies heavily on the age and provenance of Cenozoic sediments preserved in the Qaidam basin. Here, we present evidence in the northern plateau for a considerably younger inception and evolution of the Qaidam basin, based on magnetostratigraphies combined with detrital apatite fission-track ages that date the basin fills to be from ca. 30 to 4.8 Ma. Detrital zircon-provenance analyses coupled with paleocurrents reveal that two-stage growth of the Qilian Shan in the northeastern margin of the Tibetan Plateau began at ca. 30 and at 10 Ma, respectively. Evidence for ca. 30 and 10 to 15 Ma widespread synchronous deformation throughout the Tibetan Plateau and its margins suggests that these two stages of outward growth may have resulted from the removal of mantle lithosphere beneath different portions of the Tibetan Plateau.

Qaidam basin | magnetostratigraphy | northeastern Tibetan Plateau

Geodynamic processes in the interior of broad, high-elevation orogenic plateaus have a pronounced effect on the outward growth of those plateaus over time (1–3). The Cenozoic collision of India and Eurasia has built the high-elevation Tibetan Plateau (>4.5 km) that extends almost 2,000 km from the Himalaya into central Asia. Resolving the geodynamic processes that controlled development of high topography in Tibet underpins understanding the nature of intracontinental deformation (3–5), mechanisms of surface uplift of orogenic plateaus (2, 6, 7), and their impact on regional and global climate change (8, 9). In the northeastern Tibetan Plateau, numerous Cenozoic basins are separated by narrow mountain ranges (Fig. 1A); deformation within the basins and growth of the intervening mountain ranges (10) have led some to propose geodynamic mechanisms for the outward and upward growth of the Tibetan Plateau and its northeastern margin including: 1) progressive, south-to-north propagation in stepwise fashion along lithospheric strike-slip faults (3, 11); 2) lateral flow of middle-lower crust from the main body of the Tibetan Plateau into its margins (2, 6, 12); and 3) the removal of mantle lithosphere beneath all or part of the Tibetan Plateau (1, 4, 13). All of these models rely heavily on the ages of Cenozoic sediments preserved in Tibetan basins.

As the largest Cenozoic basin with >10-km-thick deposits in the northeastern Tibetan Plateau (14), the Qaidam basin's inception, development, and extinction provides critical insights into the timing, processes, and mechanisms of Tibetan Plateau growth. Here, we combine detrital zircon provenance with magnetostratigraphies and detrital apatite fission-track (DAFT) from the Hongshan East and West sections in the northern basin margin (Fig. 1B) to decipher the inception of Cenozoic

sedimentation in the Qaidam basin and the emergence of ranges around it. Constrained by youngest detrital apatite fission-track peak ages, our paleomagnetic investigation provides a temporal framework for the Qaidam basin depositions spanning from ca. 30 to 4.8 Ma, within which detrital zircon provenance analysis reveals the ca. 30 Ma initial growth of the South Qilian Shan, followed by a second accelerated growth of the entire Qilian Shan since ca. 10 Ma. We compare this growth history with major deformational events within the central and northern Tibetan Plateau to demonstrate that pulses of outward growth on the northern margin of Tibetan Plateau occurred during pulses of rapid uplift in the plateau's interior. Such pulsed uplift is consistent with multistage removal of dense lower lithosphere as an important process governing the upward and outward growth of orogenic plateaus in collisional tectonic settings.

Geologic Setting of the Qaidam Basin

The Qaidam basin is the largest triangular synclinal basin situated in the northeastern Tibetan Plateau (14, 15). The basin is defined by the East Kunlun Shan to the south, the Qilian Shan to the north, and the Altyn Tagh Range, as well as Altyn Tagh Fault (ATF), to the west (Fig. 1B). The basin has now been deformed to form a series of WNW–ESE striking folds

Significance

The formation of the Qaidam basin in the northeastern Tibet marked the onset of crustal deformation that propagated from the Indo-Asia collision zone to the northern margins of the Tibetan Plateau during the Cenozoic time. This paper presents magnetostratigraphies constrained by apatite fission-track ages that document the formation of the Qaidam basin at ca. 30 Ma, much younger than previous estimates of 65 to 50 Ma. Armed with chronology, the Qaidam basin–provenance analyses reveal pulsed deformation of the northeastern margin of the Tibetan Plateau beginning first at ca. 30 Ma and subsequently at ca. 10 Ma, timing suggesting close links to the removal of the mantle lithosphere beneath different portions of the Tibetan Plateau.

Author contributions: W.W. and P.Z. designed research; W.W., Z.Z., J.P., Y.W., D.Z., W.Z., and H.Z. performed research; W.W., C.N.G., C.L., and D.Z. analyzed data; and W.W., P.Z., and C.N.G. wrote the paper.

The authors declare no competing interest.

This article is a PNAS Direct Submission.

This article is distributed under [Creative Commons Attribution-NonCommercial-NoDerivatives License 4.0 \(CC BY-NC-ND\)](https://creativecommons.org/licenses/by-nc-nd/4.0/).

¹To whom correspondence may be addressed. Email: wangweitao@mail.sysu.edu.cn.

This article contains supporting information online at <http://www.pnas.org/lookup/suppl/doi:10.1073/pnas.2120364119/-DCSupplemental>.

Published February 15, 2022.

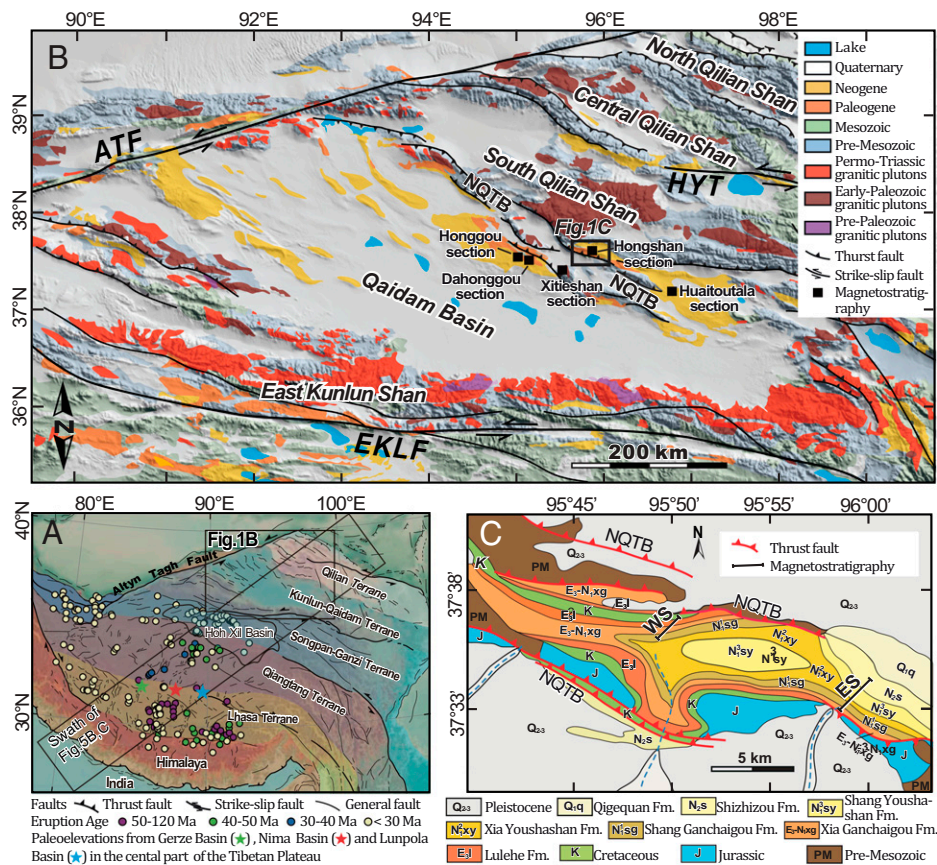


Fig. 1. (A) Regional shaded relief map of the Tibetan Plateau showing major faults, terranes, volcanic rock ages, and paleoelevation study sites. The black rectangles outline extent of *B* and the swath of Fig. 5 *B* and *C*. (B) Generalized tectonic and topographic map of the East Kunlun Shan, Qilian Shan, and the Qaidam basin with magnetostratigraphic section locations (solid squares) in the north margin of the basin. ATF, Altyn Tagh fault; EKLF, East Kunlun fault; NQTB, North Qaidam thrust belt; and HYT, Haiyuan fault. (C) Geological map of the Hongshan region [modified after Qinghai Bureau of Geology and Mineral Resources (17)]. Shown are the distributions of Cenozoic stratigraphic units (Lulehe, Xia Ganchaigou, Shang Ganchaigou, Xia Youshashan, Shang Youshashan, Shizigou, and Qigequan formations) in the study area and Hongshan West section (WS) as well as Hongshan East section (ES).

and thrust faults, such as the Northern Qaidam thrust belt (NQTB) on the northern basin margin (Fig. 1*B*). Erosion across these folds and faults has exposed many of the stratigraphic successions in the basin. Cenozoic strata of the Qaidam basin have been subdivided into seven, progressively younger stratigraphic units: the Lulehe, Xia Ganchaigou, Shang Ganchaigou, Xia Youshashan, Shang Youshashan, Shizigou, and Qigequan formations (14, 16, 17). The depositional age of the Lulehe Formation was previously designated as early Eocene based on sparse pollen and ostracode assemblages (14, 17), and the overlying Xia Ganchaigou to Shizigou formations were assigned Eocene to Pliocene ages (14, 18, 19). However, our magnetostratigraphies and DAFT dates the Lulehe Formation to Oligocene, rather than Eocene (Fig. 1*C*). Hence, the onset of Cenozoic deposition is much younger than previously assumed.

Our sampled sections are referred to as the Hongshan West and the Hongshan East sections, which are exposed in the north and south flanks of a syncline, respectively, related to the NQTB (Fig. 1*C*). The West section spans ~2,200 m from 37°36'52"N, 95°49'52"E to 37°35'50"N, 95°48'43"E, and the East section initiates at 37°32'17"N, 96°00'46"E and ends at 37°33'17"N, 96°2'18"E. The two sections are at a distance of ~12 km along the same exposed anticline (Fig. 1*C*). The West section contains the Lulehe, Xia Ganchaigou, and Shang Ganchaigou formations, whereas the Shang Ganchaigou to Shizigou formations are exposed within the East section (Fig. 1*C*). In the West section, the almost 800-m-thick Lulehe Formation

unconformably overlies Cretaceous strata and is characterized by dark red alluvial conglomerates intercalated with red sandstones: characteristics lithostratigraphically consistent with its typical section (14, 17), which is located at ~100 km west of the Hongshan West section. Overlying the Lulehe Formation, stratigraphic units of the Xia Ganchaigou to Shizigou formations comprise thick, greenish-gray sandstone, red mudstone, siltstone, and conglomerates (Fig. 2 and *SI Appendix*, Figs. 1 and 2). Strata of the West and East sections are described in detail in the *SI Appendix*.

Detrital Apatite Fission-Track

To determine the onset of formation of the Qaidam basin, we dated the stratigraphic successions that include the oldest deposits in the basin. A total of 14 DAFT samples were collected from the Hongshan West and East sections (Fig. 2). The DAFT grain ages were decomposed into statistically significant age peaks using the radial plotter method (20) and binomial peak-fitting method (21) (Fig. 2 and *SI Appendix*, Table 1 and Figs. 4 and 5). We rule out partial resetting by postdepositional burial for the Hongshan DAFT samples (*Methods*). These apatite grains, therefore, preserve cooling ages of their source rocks, and their youngest peak ages can be used to constrain the lower bound of depositional ages of the samples. The youngest peak ages of 14 samples in the sections range from 69.4 to 28.2 Ma (Fig. 2 and *SI Appendix*, Table 1). In particular, samples W401 and W309 in the lower and upper parts of the

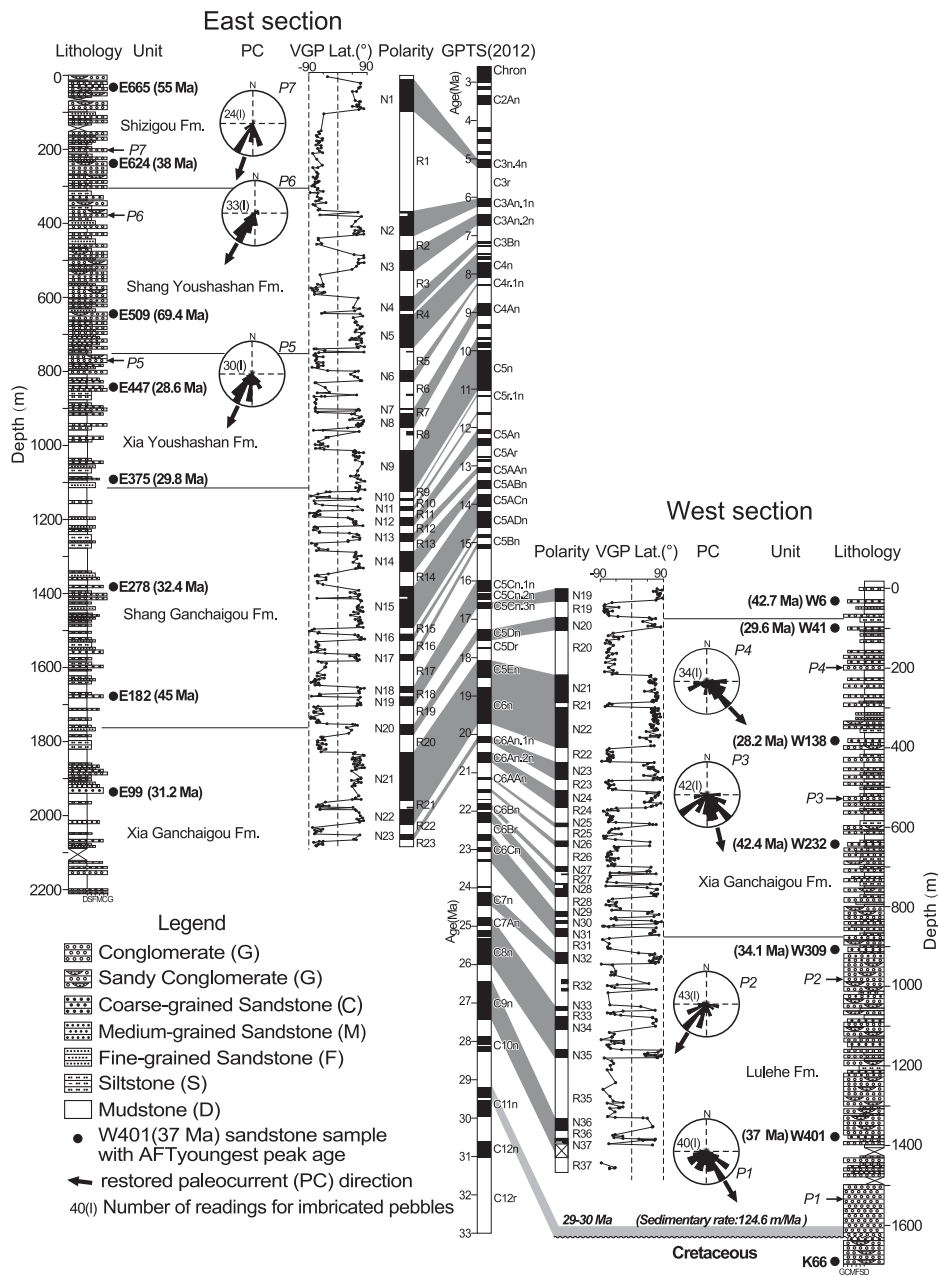


Fig. 2. Correlations of observed magnetostratigraphy to the GPTS (2012) (25, 26). Sites of the detrital apatite fission-track samples (with youngest fission-track peak ages), detrital zircon U-Pb samples, and paleocurrent indicators are plotted on the *Right* or *Left* of the stratigraphic columns. The youngest peak ages of detrital AFT from basal conglomerates constrained the magnetostratigraphies to younger than 37 Ma.

Lulehe Formation along the West section yield the youngest peak ages of 37 and 34 Ma, suggesting the lower and upper parts of the Lulehe Formation must be younger than 37 and 34 Ma, respectively (Fig. 2).

Magnetostratigraphy

Paleomagnetic analyses (see *Methods*) were performed on both the West and East sections. After removing the soft secondary components of magnetization, characteristic remanence (ChRM) directions in the sections were obtained (SI Appendix, Fig. 10 and Table 2). Rock magnetic measurements identify that the ChRM directions in the Hongshan West and East sections are held in magnetite and hematite (SI Appendix, Figs. 6–9). All of the accepted ChRM directions of the sections

pass a class reversal test at 95% confidence level (SI Appendix, Fig. 11) (22). Further analysis applying the progressive unfolding of Tauxe and Watson (23) shows the best grouping of the overall mean directions occurs at 98 to 101% (SI Appendix, Fig. 12). Both positive reversal and fold tests demonstrate that the ChRM directions of the Hongshan West and East sections are primary.

In the Qaidam basin, the Honggou mammalian fauna was discovered in the Shang Ganchaigou Formation along the Honggou section (Fig. 3E). It contains abundant biochronologically useful mammalian fossils of the late Middle Miocene; that is, the late Middle Miocene Tunggur Age of the Chinese Land Mammal Ages corresponding to mammalian chronozones MN7/8 of the European Land Mammal Ages (24). As *Detrital Apatite Fission-Track* mentioned, the DAFT ages state that the

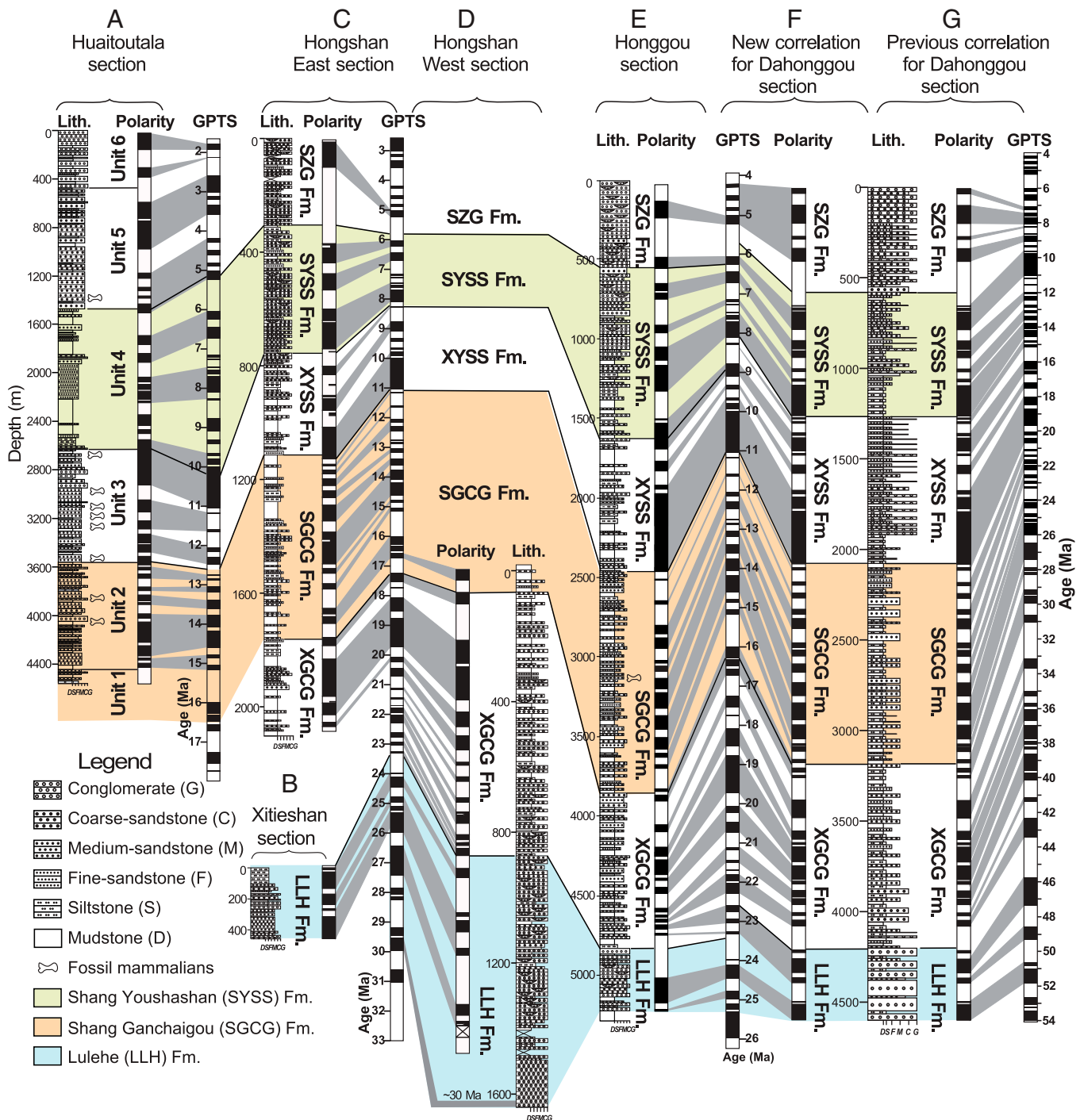


Fig. 3. Correlations (from Left to Right) among GPTS (2012) of the stratigraphic sections Huitoutala section (A) (16), Xitieshan section (B) (28), Hongshan East (C) and West (D) sections (this study), Honggou section (E) (24), and Dahonggou section (F and G) (27), where both original and recorrelated sequences are depicted. The ages of the basal Lulehe Formation in these sections along the north Qaidam basin margins appears regionally consistent in the Oligocene.

Lulehe Formation in the Hongshan West section is younger than 37 Ma. These constraints enable unequivocal correlation of the Hongshan West and East magnetic polarity sequences to the geomagnetic polarity time scale (GPTS) (25, 26). The recognized magnetic polarity sequences of the Hongshan West and East sections were therefore anchored to Chrons C9n to C5Cn.3n (27.8 – 16.5 Ma) and Chrons C6AAn.1n to C3n.4n (21.3 to 4.8 Ma), respectively (Fig. 2). Along the West section, ~180 m of conglomerate in the base were not dated because of the coarse-grained nature of conglomerates without any fine-

grained sediments. Extrapolating downward ~180 m at a sediment accumulation rate of 12.4 cm/kyr (estimated between 1400 and 0 m in the West section) yields a basal age of ca. 30 Ma (Fig. 2). The details for magnetostratigraphic correlations are presented in the *SI Appendix* and they date Cenozoic deposits in the northern Qaidam basin between ca. 30 and 4.8 Ma.

The Hongshan magnetostratigraphic correlations refine the onset of the Qaidam basin fill to ca. 30 Ma: much younger than the Paleogene basin formation interpreted by previous studies. To the southwest of the Hongshan sections about 60 km, the

Dahonggou magnetostratigraphic section (see Fig. 1B for the location) that encompasses the Lulehe to Shizigou formations was previously estimated to span ca. 52 to 7 Ma (Fig. 3G) based on preserved palynological assemblages, ostracod assemblages, and leaf fossils (27). However, the significant uncertainties in dating Cenozoic sediments using pollens, ostracods, and leaves in the Qaidam basin hinder the definitive and reliable correlations between the Dahonggou magnetostratigraphy and GPTS. According to the Honggou mammalian fauna and magnetozone pattern, we are able to refine the Dahonggou magnetostratigraphy-to-GPTS correlation to span 24.5 to 4.2 Ma (Fig. 3F). The north basin margin magnetostratigraphies (see Fig. 1B for the locations) including the Huaitoutala (16), Xitieshan (28), Honggou (24), and Dahonggou (27) sections were further correlated to the Hongshan sections (Fig. 3). These magnetostratigraphies are each consistent with Qaidam basin formation at ca. 30 Ma.

Provenance of the Qaidam Basin Fill

Constrained by the chronostratigraphic framework, detrital zircon-age spectra and paleocurrent indicators were used to assess sediment provenance. We present detrital zircon-age results from nine sandstone samples collected in the Hongshan West and East sections and compare these ages with their potential source zircon ages (Figs. 2 and 4 and *SI Appendix, Table 3*). Around the Qaidam basin, the East Kunlun Shan to the south and the Qilian Shan to the north serve as the two most likely source regions. The Qilian Shan consists dominantly of lower Paleozoic granitic rocks and Pre-Mesozoic sedimentary rocks with main age clusters of 410 to 510 Ma and 700 to 1,100 Ma. The remaining ages are scattered between 1,100 Ma and 3,000 Ma, with many results in 1,700 to 2,000 Ma and 2,200 to 2,500 Ma (24, 29) (Fig. 4A). In contrast, zircons from the East Kunlun Shan are dominated (~50%) by 200- to 300-Ma ages (24, 29) (Fig. 4K); these ages are rarely detected in the Qilian Shan to the north of the Qaidam basin. Older zircon grains in the East Kunlun Shan are mainly scattered between 300 and 1,600 Ma with a minor peak in 380 to 480 Ma (Fig. 4K).

In our sections, the Cretaceous sample K66 (Fig. 4J) and three 19 to 12 Ma strata samples (E99, W6, and E375) (Fig. 4D–F) share similar zircon age spectra. They are characterized by a major age-probability peak at ca. 250 Ma and four minor peaks at ca. 440, ca. 830, ca. 1,880, and ca. 2,450 Ma (Fig. 4D–F and *J* and *SI Appendix, Table 3*). Because the Qilian Shan lacks ca. 250-Ma zircon-peak age and the East Kunlun Shan lacks zircon-peak ages > 1,000 Ma, the presence of strong 200- to 300-Ma and >1,000-Ma age populations in these samples makes both the East Kunlun Shan and the Qilian Shan plausible sources for the Cretaceous and early-middle Miocene deposits.

The three 28 to 21 Ma samples (W401, W309, and W232) were collected from sandstone lenses within the pebble conglomerates along the Hongshan West section (Fig. 2). Sedimentary textures indicate these rocks were alluvial fan/braided river depositions near eroding source region (*SI Appendix, Fig. 2A*). The conglomerates within the Hongshan West section contain SW- to SE-directed paleocurrents (Fig. 2), indicating paleoflow away from the Qilian Shan.

The three samples (W401, W309, and W232) also yield a unimodal ca. 445-Ma peak, which accounts for 75 to 85% of the total dated grains (Fig. 4G–I). These narrow zircon-age spectra are similar to those of Early Paleozoic granitic plutons in the Qilian Shan region. Actually, a huge Early Paleozoic granitic pluton (>500 km²) were exposed in the southernmost Qilian Shan adjacent the Hongshan section (Fig. 1B). Based on the similar zircon-ages, south-trending paleocurrents and near-source characteristics of 28 to 21 Ma conglomerates, we

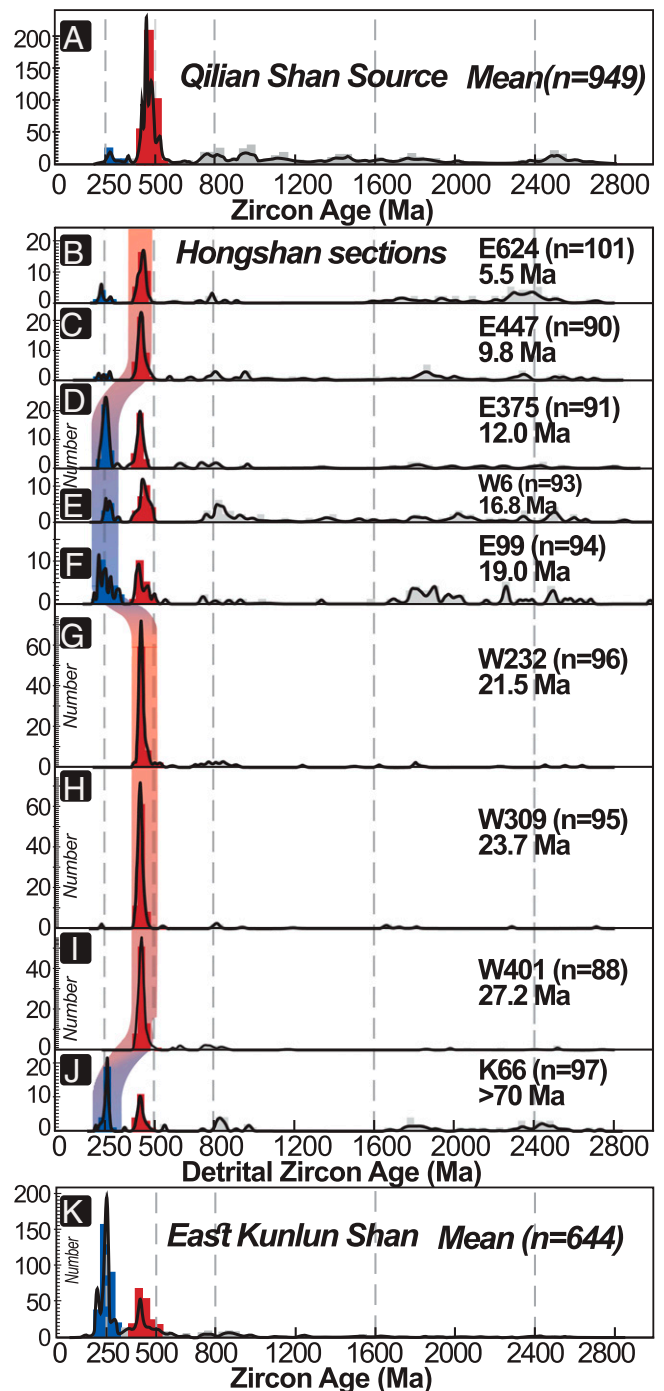


Fig. 4. Detrital zircon U-Pb age probability distributions from source terranes in the Qilian Shan (A), East Kunlun Shan (K), and zircon-age distributions of sandstones (B–J) from magnetostratigraphic horizons within the Hongshan West and East sections (locations of samples are shown in Fig. 2). Radioisotope database is presented in *SI Appendix, Table 3*. Detrital zircon U-Pb age spectra are depicted as age-probability-density functions (thick lines) and age histograms.

suggest that the 30 to 21 Ma strata in the study area were most likely sourced from the South Qilian Shan.

Our 10 to 5 Ma samples (E447 and E624) were collected from the Xia Youshashan-Shizigou formations along the Hongshan East section (Fig. 2). Within these stratigraphic units, general south-directed paleocurrents were defined by imbricated clasts (Fig. 2). The samples E447 and E624 follow nearly the same

age spectra, which are dominated by detrital zircon ages between 410 and 480 Ma (Fig. 4 B and C). Zircon ages < 410 Ma only account for ~5% of the total dated grains; whereas clustered grain ages > 480 Ma mimic those of zircons from the modern Qilian Shan (Fig. 4A).

Combined with paleocurrent and stratigraphic data, comparison of zircon-age spectra from the Qaidam basin fill to its potential source regions reveals that the Qilian Shan served as the dominant source of sediment to the Qaidam basin during the initial stages of deposition between 30 to 20 Ma and after ca. 10 Ma (Fig. 4). Mixed sources from the East Kunlun Shan and Qilian Shan provided sediment to the basin during the Cretaceous and between 20 and 10 Ma.

Discussion: Coeval Plateau-Wide Uplift and Associated Borderland Deformation

Our chronology of basin strata proves the onset of deposition in the Qaidam basin to ca. 30 Ma: a timing consistent with previously described magnetostratigraphies in the north Qaidam basin (Fig. 3). These data indicate a much younger (Oligocene) inception age of the Qaidam basin compared to previously inferred sedimentary initiation at 65 to 55 Ma (14, 17, 27). Conglomerates

of the Lulehe Formation in the northern margin of the basin were derived directly from adjacent granitic plutonic sources in the southern Qilian Shan, corroborating that the southern Qilian Shan had pulsed to develop considerable structural relief by ca. 30 Ma. This result is consistent with multiple lines of evidence indicating tectonic deformation and surface uplift (Fig. 5A) at that same time, for example, the onset of exhumation driven by range-bounding fault systems in the East Kunlun Shan at ca. 30 Ma (30–32), Oligocene activation of the ATF (33), uplift of the West Qinling since ca. 30 Ma (34), onsets of most Cenozoic sedimentary basins in the northeastern Tibetan Plateau at ca. 30 Ma (24, 35–37), and the presence of pollen from “high-altitude vegetation” in the Xining basin at ca. 34 Ma (38).

Further south, a rapid surface uplift appeared to occur in central Tibet at ca. 30 Ma. Although the oxygen isotopes in sediments from the southern Tibetan Plateau probably have been reset (39), the oxygen isotopes of pedogenic carbonates from the central Tibet (Lhasa, Qiangtang terranes; Fig. 1A) seem to be unaltered and useful for paleoelevation reconstruction. Recent carbonate $\delta^{18}O$ and fossil foraminifera results from the northern Lhasa terrane of the central Tibetan Plateau (Fig. 1A) suggest that paleoelevation increased by 2 km between late Eocene and Oligocene time (ca. 36 to 25 Ma) (40–42). Fossil palm leaves

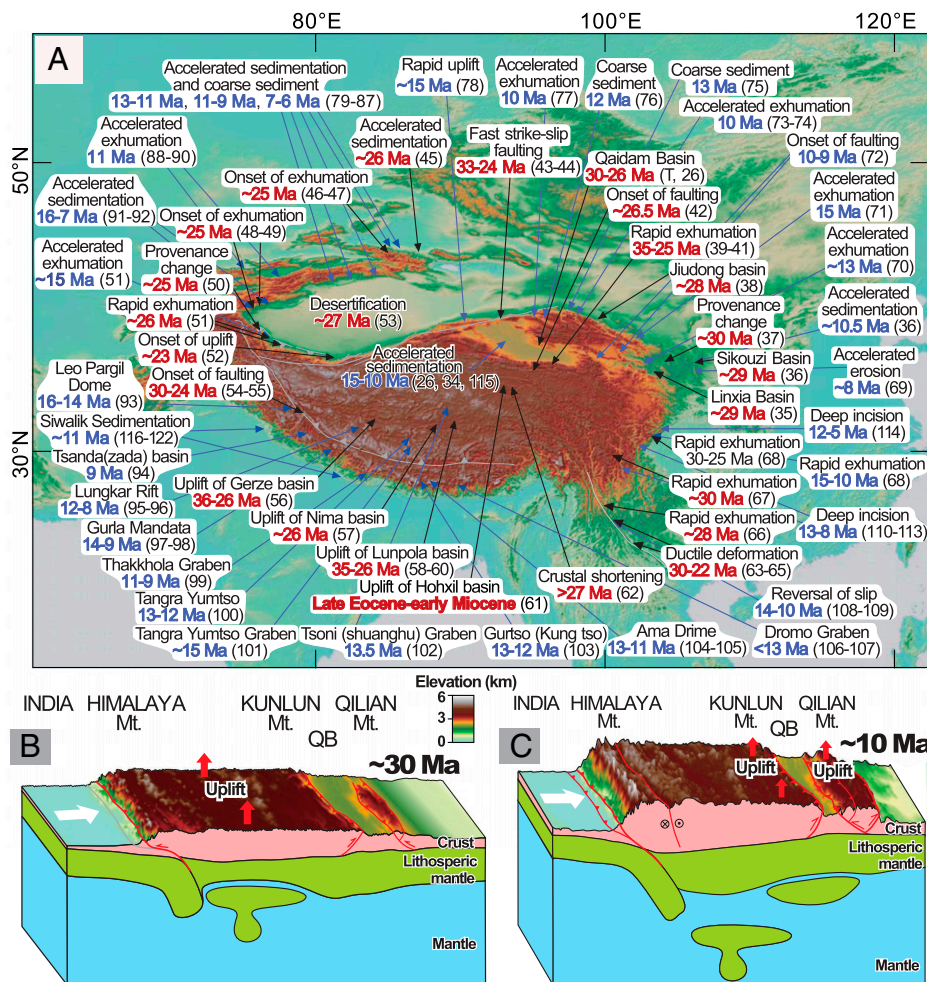


Fig. 5. (A) Distribution of the major lines of evidence for ca. 30 and 10 Ma deformation/uplift in the Tibetan Plateau. Timing (in Ma) of the initiation and duration of the deformation inferred from integrating geothermochronology, magnetostratigraphy, biostratigraphy-constrained sediments, and structure data. The marks represent references, which are shown in *SI Appendix, Table 4* in detail. (B) Schematic tectonic diagram illustrates the removal of mantle lithosphere beneath south and central Tibet driving plateau surface uplift and outward growth at ca. 30 Ma. (C) Following lithospheric thickening, convective instability triggers removal of lithospheric mantle beneath northern Tibet, causing the second-stage deformation and growth of the plateau to its recent northeastern margin in ca. 10 Ma.

combined with updated chronology of the Lunpola basin also indicate the elevation of the central Tibetan Plateau increased from <2.3 km to 3.5 to 4.5 km near ca. 26 Ma (43, 44). Fig. 5A (*SI Appendix, Table 4*) summarizes multiple lines of the published evidence suggesting that coeval plateau-wide uplift and associated borderland deformation began at ca. 30 Ma.

Deformation in the southern Qilian Shan in ca. 30 Ma was followed by a period of relative quiescence between ca. 20 and ca. 10 Ma. Detrital zircon age spectra from strata dated to post 10 Ma along the Hongshan East section (Fig. 4B and C) show striking similarities with those of the present-day Qilian Shan, suggesting that renewed growth of the south Qilian Shan was coeval with emergence of the central and north Qilian Shan at ca. 10 Ma. In the northern Tibet, fossil plant evidence using foliar physiognomy methods indicates that the Hoh Xil region resided between 1,400 and 2,900 m during the early Miocene, which means northern Tibet has been uplifted $\geq 1,700$ m since middle Miocene (45). Synchronous with the uplifts in the Hoh Xil and Qilian Shan, widespread tectonic deformation, range uplift, and acceleration of sedimentation took place in and around the Tibetan Plateau since the last 10 to 15 Ma (10, 46, 47). As shown in Fig. 5A (*SI Appendix, Table 4*), these plateau-wide events since 10 to 15 Ma are also characterized by synchronous topographic uplift in the interior of plateau and widespread deformation around its margins.

The pulsed synchronous upward and outward growths of the Tibetan Plateau in both ca. 30 Ma and ca. 10 Ma call for a profound geological process to dictate the coeval plateau-wide uplift and associated borderland deformation. Many models have been proposed to interpret the geodynamic processes behind the growths of the Plateau but fail to account for temporal and spatial synchronicity of the coeval upward and outward growth. The only model that could explain it successfully is the convective removal of mantle lithosphere (1, 46). Continental collision and subsequent convergence between the Indian and Eurasian continents significantly shorten and thicken Tibetan lithosphere, including both crust and mantle, which would cause Rayleigh–Taylor instability to erode the thickened mantle lithosphere and would eventually detach the thickened lithosphere to sink into the hot asthenospheric mantle. Buoyancy force associated with the dripping of mantle lithosphere would result in surface uplift to augment the potential energy and therefore to exert compressive stresses to the borderlands of the plateau causing synchronous and widespread deformation around the margins.

Chen et al. (48) use the adjoint seismic tomography method to image the geometry and spatial extent of mantle lithosphere in terms of high wave speed anomalies in the Tibetan Plateau. They find a T-shape high seismic velocity anomaly body beneath southern and central Tibetan Plateau in the depth range from ~250 to ~660 km and interpret as the foundering Tibetan lithosphere in ca. 30 Ma. In support of the lithospheric foundering, widespread potassic to ultrapotassic volcanism posterior to 26 to 30 Ma (49) has been attributed to melting of a metasomatized mantle lithosphere associated with possibly convective removal of the mantle lithosphere beneath the south and central Plateau (50). Collectively, only the lithospheric removal at ca. 30 Ma (Fig. 5B) could explain the Oligocene plateau-wide surface uplift, widespread deformation around all margins of the plateau, and the potassic to ultrapotassic volcanism (Fig. 5B). During this stage deformation, the early Cenozoic (>30 Ma) proto-Qilian Shan was pulsed to thrust the Qaidam basin forming the paleo-boundary of the northeastern Tibetan Plateau (Fig. 5B), so that the ca. 445 Ma plutons started to serve as sources for the Lulehe conglomerate (Figs. 1B and 4).

Tomographic results also show a fuzzy high seismic velocity body beneath the northern Tibet in the depth between 100 and 180 km, which could be interpreted as another piece of the removed mantle lithosphere (49). Rapid surface uplift and

plateau-wide synchronous tectonic deformation (Fig. 5A) clearly suggest that this removed piece of the mantle lithosphere underneath the northern Tibet, together with the continuous sink of previous one, might have triggered upward and outward growth of the Tibetan Plateau since ca. 10 Ma (Fig. 5C). The coeval surface uplift and widespread deformation in the Qilian Shan probably are the consequence of this mantle lithospheric removal (Fig. 5C). We, therefore suggest that two-stage removal of thickened mantle lithosphere beneath different parts of the Tibetan Plateau drove the pulsed upward and outward growth of the Plateau to its recent margins since the late Paleogene.

Methods

Paleomagnetic Dating. A total of 452 and 675 sites core paleomagnetic samples were, respectively, collected from the Hongshan West and East sections at intervals of 2 to 3 m, respectively, to acquire magnetostratigraphies. All drilled core samples were cut into 2 cm in length before going on the magnetometer. After natural remanent magnetization measurements, systematic stepwise thermal demagnetization in 15 to 20 discrete steps was applied for all of the specimens by using a TD-48 oven at temperatures ranging from 20 to 680/690 °C. Magnetic remanence was measured with a 2G cryogenic magnetometer at the Paleomagnetism and Geochronology Laboratory of the Institute of Geology and Geophysics, Chinese Academy of Sciences. The ChRM directions were determined by principal component analysis. A total of 422 samples from the West section and 544 samples from the East section gave reliable ChRM directions (*SI Appendix, Fig. 3 and Table 2*). Details of magnetostratigraphic analysis and test are described in the *SI Appendix*.

Apatite Fission Track (AFT) Dating. AFTs were measured using the external detector method, and the AFT ages were calculated by the zeta-calibration method. Age-calibration standards are Durango apatite and Fish Canyon apatite. DAFs document their source rocks cooling ages if the tracks do not reset by postdepositional burial. For the basin sedimentary process, the source rocks first underwent erosion/cooling to become detritus, and then the detritus was transported and deposited. The cooling ages of basin source rocks therefore are older than the ages of corresponding detritus deposition. Generally, the basin detritus eroded from multiple sources, and the DFAT ages were mixed ages. These ages can be decomposed to different peak-ages, the youngest peak age probably represent the youngest stage of basin source rocks cooling/exhumation. Thus, the youngest peak-ages can be used to constrain the lower bound of sample depositional age.

If the DFAT were reset/partially reset by postdepositional burial, the ages 1) become a single age population; 2) become younger and younger through burial into the deeper depth; and 3) fission tracks were shortened. Partial resetting of the Hongshan DAFs was ruled out because of relatively long lengths of individual fission tracks, lack of decreasing trends in the mean track-length with depth (11.8 to 12.9 μm : *SI Appendix, Fig. 3*), and lack of gradually younger trends of ages with depth. Therefore, the youngest peak-ages of our 14 samples from the Hongshan West and East sections constrain the lower bound of depositional ages of the corresponding samples. The details for AFT dating are described in the *SI Appendix*.

Detrital Zircon U-Pb Dating. Detrital zircon U-Pb dating was analyzed by an Agilent 7500a inductively coupled plasma mass spectrometer equipped with a 193-nm laser excitation system. The field and laboratory techniques about zircon U-Pb dating are described in detail in the *SI Appendix*.

Data Availability. The measured paleomagnetic data in this paper are available in the Magnetism Information Consortium (MagIC), (earthref.org/MagIC/19398/ac79503f-2329-4b78-a3e3-d43b7ec3bb8f/), and the results are also provided in *SI Appendix, Table 2*. The detrital apatite fission-track data, detrital Zircon U-Pb data, and summarized timing (in Ma) of the tectonic deformation inferred from sedimentation, geothermochronology, and structure data are provided in *SI Appendix, Tables 1, 3, and 4*, respectively. All other study data are included in the article and/or *SI Appendix*.

ACKNOWLEDGMENTS. This research was jointly supported by the Second Tibetan Plateau Scientific Expedition and Research Program (Grant 2019QZKK0901), the National Natural Science Foundation of China (Grants 42030301, 41888101, and 41872204), and Guangdong Province Introduced Innovative R&D Team of Geological Processes and Natural Disasters (Grant 2016ZT06N331). We thank the editor and two reviewers' comments that improved the clarity of the paper significantly. We thank Keng Huang for assistance with magnetostratigraphic sample collection and Rixiang Zhu for sample measurement and analysis.

1. P. Molnar, P. England, J. Martinod, Mantle dynamics, uplift of the Tibetan Plateau, and the Indian monsoon. *Rev. Geophys.* **31**, 357–396 (1993).
2. L. H. Royden *et al.*, Surface deformation and lower crustal flow in eastern Tibet. *Science* **276**, 788–790 (1997).
3. P. Tapponnier *et al.*, Oblique stepwise rise and growth of the Tibet Plateau. *Science* **294**, 1671–1677 (2001).
4. P. England, G. Houseman, Finite strain calculations of continental deformation: 2. Comparison with the India-Asia collision zone. *J. Geophys. Res. Solid Earth* **91**, 3664–3676 (1986).
5. L. H. Royden, B. C. Burchfiel, R. D. van der Hilst, The geological evolution of the Tibetan Plateau. *Science* **321**, 1054–1058 (2008).
6. M. K. Clark, L. H. Royden, Topographic ooze: Building the eastern margin of Tibet by lower crustal flow. *Geology* **28**, 703–706 (2000).
7. E. Wang *et al.*, Two-phase growth of high topography in eastern Tibet during the Cenozoic. *Nat. Geosci.* **5**, 640–645 (2012).
8. G. Dupont-Nivet *et al.*, Tibetan Plateau aridification linked to global cooling at the Eocene-Oligocene transition. *Nature* **445**, 635–638 (2007).
9. Z. T. Guo *et al.*, Onset of Asian desertification by 22 Myr ago inferred from loess deposits in China. *Nature* **416**, 159–163 (2002).
10. D. Y. Yuan *et al.*, The growth of northeastern Tibet and its relevance to large-scale continental geodynamics: A review of recent studies. *Tectonics* **32**, 1358–1370 (2013).
11. B. Meyer *et al.*, Crustal thickening in Gansu-Qinghai, lithospheric mantle subduction, and oblique, strike-slip controlled growth of the Tibet plateau. *Geophys. J. Int.* **135**, 1–47 (1998).
12. P. Bird, Lateral extrusion of lower crust from under high topography in the isostatic limit. *J. Geophys. Res. Solid Earth* **96**, 10275–10286 (1991).
13. T. M. Harrison, P. Copeland, W. S. Kidd, A. Yin, Raising Tibet. *Science* **255**, 1663–1670 (1992).
14. A. Yin, Y. Q. Dang, M. Zhang, X. H. Chen, M. W. McRivette, Cenozoic tectonic evolution of the Qaidam basin and its surrounding regions (Part 3): Structural geology, sedimentation, and regional tectonic reconstruction. *Geol. Soc. Am. Bull.* **120**, 847–876 (2008).
15. A. Bally *et al.*, “Notes on sedimentary basins in China; Report of the American sedimentary basins delegation to the people’s Republic of China” (Open-File Report 86-327, US Geological Survey, 1986).
16. X. Fang *et al.*, High-resolution magnetostratigraphy of the Neogene Huaitoutala section in the eastern Qaidam basin on the NE Tibetan Plateau, Qinghai Province, China and its implication on tectonic uplift of the NE Tibetan Plateau. *Earth Planet. Sci. Lett.* **258**, 293–306 (2007).
17. Qinghai Bureau of Geology and Mineral Resources, *Regional Geology of Qinghai Province* (Geological Publishing House, Beijing, China, 1990), ch. 11, part I, pp. 206–226.
18. Z. Sun *et al.*, Magnetostratigraphy of Paleogene sediments from northern Qaidam basin, China: Implications for tectonic uplift and block rotation in northern Tibetan Plateau. *Earth Planet. Sci. Lett.* **237**, 635–646 (2005).
19. H. Chang *et al.*, Magnetostratigraphy of Cenozoic deposits in the western Qaidam basin and its implication for the surface uplift of the northeastern margin of the Tibetan Plateau. *Earth Planet. Sci. Lett.* **430**, 271–283 (2015).
20. P. Vermeesch, RadialPlotter: A Java application for fission track, luminescence and other radial plots. *Radiat. Meas.* **44**, 409–410 (2009).
21. M. T. Brandon, Decomposition of mixed grain age distributions using BINOMFIT. *On Track* **24**, 13–18 (2002).
22. P. McFadden, M. McElhinny, Classification of the reversal test in palaeomagnetism. *Geophys. J. Int.* **103**, 725–729 (1990).
23. L. Tauxe, G. Watson, The fold test: An Eigen analysis approach. *Earth Planet. Sci. Lett.* **122**, 331–341 (1994).
24. W. Wang *et al.*, Expansion of the Tibetan Plateau during the Neogene. *Nat. Commun.* **8**, 15887 (2017).
25. F. Hilgen, L. Lourens, J. Van Dam, *The Neogene Period in Geologic Time Scale 2012*, F. M. Gradstein *et al.*, Eds. (Elsevier, 2012), vol. 2, chap. 29, pp. 923–978.
26. N. Vandenbergh *et al.*, *The Paleogene Period in Geologic Time Scale 2012*, F. M. Gradstein *et al.*, Eds. (Elsevier, 2012), vol. 2, chap. 28, pp. 855–921.
27. J. L. Ji *et al.*, High-resolution magnetostratigraphic study of the Paleogene-Neogene strata in the northern Qaidam basin: Implications for the growth of the northeastern Tibetan Plateau. *Gondwana Res.* **46**, 141–155 (2017).
28. X. Ke *et al.*, Magnetostratigraphy and anisotropy of magnetic susceptibility of the Lulehe Formation in the northeastern Qaidam basin. *Acta Geol. Sin.* **87**, 576–587 (2013).
29. M. A. Bush, J. E. Saylor, B. K. Horton, J. S. Nie, Growth of the Qaidam basin during Cenozoic exhumation in the northern Tibetan Plateau: Inferences from depositional patterns and multiproxy detrital provenance signatures. *Lithosphere* **8**, 58–82 (2016).
30. M. K. Clark, K. A. Farley, D. Zheng, Z. Wang, A. R. Duvall, Early Cenozoic faulting of the northern Tibetan Plateau margin from apatite (U–Th)/He ages. *Earth Planet. Sci. Lett.* **296**, 78–88 (2010).
31. C. Mock, N. O. Arnaud, J. M. Cantagrel, An early unroofing in northeastern Tibet? Constraints from Ar⁴⁰/Ar³⁹ thermochronology on granitoids from the eastern Kunlun Range (Qinghai, NW China). *Earth Planet. Sci. Lett.* **171**, 107–122 (1999).
32. C. Li *et al.*, Late Oligocene tectonic uplift of the East Kunlun Shan: Expansion of the northeastern Tibetan Plateau. *Geophys. Res. Lett.* **48**, e2020GL091281 (2021).
33. B. D. Ritts, Y. Yue, S. A. Graham, Oligocene-Miocene tectonics and sedimentation along the Altyn Tagh Fault, northern Tibetan Plateau: Analysis of the Xorkol, Subei, and Aksay basins. *J. Geol.* **112**, 207–229 (2004).
34. W. Wang *et al.*, Pulsed growth of the West Qinling at ~30 Ma in northeastern Tibet: Evidence from Lanzhou basin magnetostratigraphy and provenance. *J. Geophys. Res. Solid Earth* **121**, 7754–7774 (2016).
35. W. Wang *et al.*, Tertiary basin evolution along the northeastern margin of the Tibetan Plateau: Evidence for basin formation during Oligocene transtension. *Geol. Soc. Am. Bull.* **125**, 377–400 (2013).
36. X. M. Fang, C. Garzzone, R. Van der Voo, J. J. Li, M. J. Fan, Flexural subsidence by 29 Ma on the NE edge of Tibet from the magnetostratigraphy of Linxia basin, China. *Earth Planet. Sci. Lett.* **210**, 545–560 (2003).
37. R. O. Lease, D. W. Burbank, B. Hough, Z. C. Wang, D. Y. Yuan, Pulsed Miocene range growth in northeastern Tibet: Insights from Xunhua basin magnetostratigraphy and provenance. *Geol. Soc. Am. Bull.* **124**, 657–677 (2012).
38. G. Dupont-Nivet, C. Hoorn, M. Konert, Tibetan uplift prior to the Eocene-Oligocene climate transition: Evidence from pollen analysis of the Xining basin. *Geology* **36**, 987–990 (2008).
39. J. Quade *et al.*, Resetting southern Tibet: The serious challenge of obtaining primary records of paleoaltimetry. *Global Planet. Change* **191**, 103194 (2020).
40. D. B. Rowley, B. S. Currie, Palaeo-altimetry of the late Eocene to Miocene Lunpola basin, central Tibet. *Nature* **439**, 677–681 (2006).
41. Y. Wei *et al.*, Low palaeoelevation of the northern Lhasa terrane during late Eocene: Fossil foraminifera and stable isotope evidence from the Gerze basin. *Sci. Rep.* **6**, 27508 (2016).
42. P. G. DeCelles *et al.*, High and dry in central Tibet during the Late Oligocene. *Earth Planet. Sci. Lett.* **253**, 389–401 (2007).
43. T. Su *et al.*, No high Tibetan Plateau until the Neogene. *Sci. Adv.* **5**, eaav2189 (2019).
44. X. Fang *et al.*, Revised chronology of central Tibet uplift (Lunpola basin). *Sci. Adv.* **6**, 1–10 (2020).
45. B. Sun *et al.*, Early Miocene elevation in northern Tibet estimated by palaeobotanical evidence. *Sci. Rep.* **5**, 10379 (2015).
46. P. V. Yakovlev *et al.*, Slowing of India’s convergence with Eurasia since 20 Ma and its implications for Tibetan mantle dynamics. *Tectonics* **28**, TC3001 (2009).
47. W. Gan *et al.*, Initiation of clockwise rotation and eastward transport of southeastern Tibet inferred from deflected fault traces and GPS observations. *Geol. Soc. Am. Bull.* **10.1130/B36069.1** (2021).
48. M. Chen *et al.*, Lithospheric foundering and underthrusting imaged beneath Tibet. *Nat. Commun.* **8**, 15659 (2017).
49. P. V. Yakovlev *et al.*, The geochemistry of Tibetan lavas: Spatial and temporal relationships, tectonic links and geodynamic implications. *Earth Planet. Sci. Lett.* **520**, 115–126 (2019).
50. H. M. Williams, S. P. Turner, J. A. Pearce, S. P. Kelley, N. B. W. Harris, Nature of the source regions for post-collisional, potassic magmatism in southern and northern Tibet from geochemical variations and inverse trace element modelling. *J. Petrol.* **45**, 555–607 (2004).